International Journal of Solids and Structures 000 (2017) 1–14

Contents lists available at ScienceDirect

International Journal of Solids and Structures

journal homepage: www.elsevier.com/locate/ijsolstr

Experiments on imperfection insensitive axially loaded cylindrical shells

Xin Ning*, Sergio Pellegrino

Graduate Aerospace Laboratories, California Institute of Technology, 1200 E. California Blvd., Pasadena CA 91125, USA

ARTICLE INFO

Article history:
Received 4 August 2015
Revised 1 May 2016
Available online xxx

Keywords:
Wavy shell
Imperfection
Compression test

ABSTRACT

This paper presents an experimental study of imperfection insensitive composite wavy cylindrical shells subject to axial compression. A fabrication technique for making cylindrical shells with intricate shape of cross-sections has been developed. A photogrammetry technique to measure the geometric imperfections has also been developed. The behavior of the wavy shells under axial compression was predicted through simulations and measured through compression tests. Both the analyses and experiments have confirmed that the wavy shells are imperfection insensitive. Comparisons between the wavy shells and circular shells have also confirmed that introducing optimal symmetry-breaking wavy cross-sections can significantly reduce the imperfection sensitivity and improve the load-bearing capability of cylindrical shells.

1. Introduction

The buckling load of circular cylindrical shells subject to axial compression is extremely sensitive to even very small geometric imperfections (Brush and Almroth, 1975). An imperfection with amplitude of one shell thickness could reduce the buckling load to only 20% of the buckling load of the corresponding prefect shell (Koiter, 1963). This severe sensitivity to imperfections has been traditionally addressed by using overly conservative safety factors, resulting in heavy structures, or by stiffening the shells with longitudinal and circumferential stiffeners. However, stiffened shells are difficult to construct and are still somewhat sensitive to imperfections (Singer et al., 2002; Hilburger et al., 2006; Jones, 2006; Nemeth and Starnes, 1998; Scott et al., 1987). Jullien and Araar (1991) proposed an intuitively designed, nearly imperfection-insensitive cylindrical shell, called the Aster shell. This shell has a fluted cross-section consisting of identical convex arcs that prevents the amplification of imperfections under axial compression, resulting in high knockdown factor and buckling loads (Jullien and Araar, 1991; Combescure and Jullien, 2015). The Aster shell was a precursor of the present work.

Instead of following these traditional approaches, a novel approach to the design of thin cylindrical shells for axial compression was proposed by Ning and Pellegrino (2015), who designed optimal symmetry-breaking wavy cross-sections (wavy shells) that eliminate the imperfection sensitivity and maximize the buckling load for axial compression.

Ning and Pellegrino (2015) presented this approach and carried out a series of numerical studies. Three major assumptions were made in this paper. First, the critical buckling mode and one shell thickness were used as the imperfection shape and amplitude, because the actual imperfection was unknown before the shell was fabricated. Second, axial compression was applied by uniform axial load rather than uniform axial end-shortening to provide more conservative buckling loads. Third, the strength of the material was not considered. A preliminary experimental study on imperfection insensitive wavy shells was presented in Ning and Pellegrino (2013). It was found that the wavy shells that had been constructed had larger than expected mid-surface imperfections and thickness variations.

The present paper is mainly focused on the experimental validation of this new approach. A fabrication method to construct precise wavy shells has been developed. The actual mid-surface imperfections and thickness distributions were measured and were then used to predict the experimental behavior of the wavy shells. The effects of two different ways of applying axial compression on a shell and the material strength of the shell have also been considered in the present study.

The present paper is organized as follows. Section 2 outlines our method for designing imperfection insensitive wavy shells and presents a particular composite wavy shell design obtained from this method. A method for fabricating composite wavy shells is also presented. Section 3 describes a method for measuring

* Corresponding author. Current address: Department of Materials Science and Engineering, Frederick Seitz Materials Research Laboratory, University of Illinois at Urbana-Champaign, Urbana, IL 61801, USA.

E-mail addresses: ningxin87@gmail.com, xning@illinois.edu (X. Ning).

http://dx.doi.org/10.1016/j.ijsolstr.2017.02.028
0020-7683/

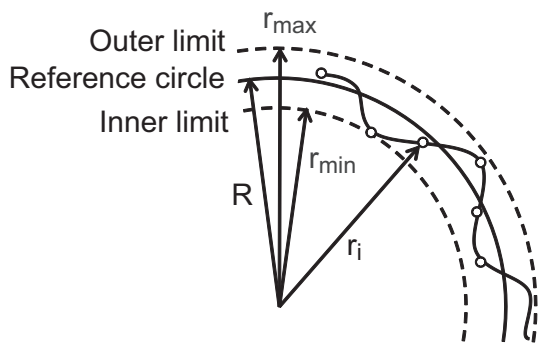

Fig. 1. Cross-section of wavy shell, defined by a finite number of control points.

geometric imperfections in wavy shells. The measured mid-surface imperfections and thickness distributions are presented, as well as the Fourier components of the mid-surface imperfections. Section 4 presents numerical predictions for these composite wavy shells subject to axial compression. The experimental setup for testing both wavy shells and circular shells and the results of these tests are presented in Section 5. Section 6 compares the results and concludes the paper.

2. Imperfection insensitive wavy cylindrical shells

This section begins by presenting an outline of the method for designing imperfection insensitive wavy cylindrical shells. The design of composite wavy shell to be tested is then presented. Lastly, a method for fabricating the composite wavy shell is presented.

2.1. Design method

Fig. 1 shows the cross-section of a wavy cylindrical shell. Imperfection insensitive wavy cylindrical shells are designed by searching with an evolutionary algorithm for optimal positions of the control points, to maximize the minimum among the buckling loads of geometrically perfect and imperfect wavy shells. The cross-section was defined by a set of control points, with a NURBS (Non-Uniform Rational B-Spline) interpolation creating a smooth, wavy curve through the control points, as shown in Fig. 1. R, r_{max}, and r_{min} are the radius of a reference circle, maximum and minimum radial positions of the control points, respectively. r_i denotes the radial position of the ith control point. The control points are defined to be radially within a distance Δr from a reference circle of radius R, where $\Delta r = r_{max} - R = R - r_{min}$. The cross-section is uniform in the axial direction.

The wavy cross-section is assumed to be mirror-symmetric with respect to the x- and y-axes, as shown in Fig. 2. Therefore, only the positions of the control points in the first quadrant are required to define the shape of the cross-section. $r_{q,i}$ and $\theta_{q,i}$ denote the radial and circumferential position of the ith control point in the qth quadrant, respectively. The control points are defined to be circumferentially equally spaced, i.e., the circumferential position of the ith control point in the first quadrant is:

$$\theta_{1,i} = \frac{\pi\,(i-1)}{2(N-1)}, \tag{1}$$

where N is the total number of control points in the first quadrant.

For any chosen candidate cross-section, the objective function for optimizing the design of the shell is defined as the minimum among the buckling loads of (i) the geometrically perfect shell (P_0), (ii) the geometrically imperfect shell obtained by superposing an imperfection of positive sign onto the perfect shell (P_+), and (iii) the shell with an imperfection of negative sign (P_-). Therefore,

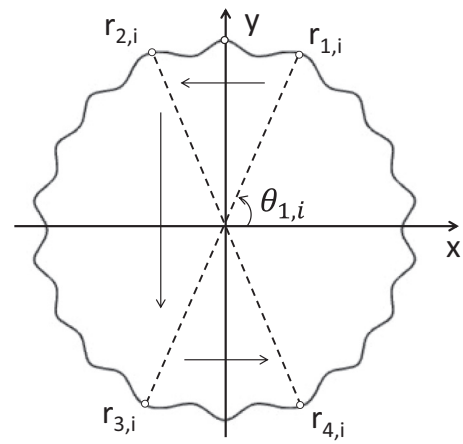

Fig. 2. Cross-section with mirror-symmetry.

$\min(P_0, P_+, P_-)$ was maximized by searching for the optimal values of the radial positions of the control points, subject to the geometric constraints described above.

The buckling loads P_0, P_+, and P_- were defined as the first limit loads on the axial load vs. displacement curves obtained from three numerical simulations carried out with the commercial finite element software Abaqus/Standard (version 6.11) Riks solver (Simulia Corp, 2011). The Evolution Strategy with Covariance Matrix Adaption (CMA-ES) (Hansen et al., 2003; Hansen, 2011; 2012) was employed to carry out the optimization. More details of the designing method can be found in Ning and Pellegrino (2015).

Three assumptions in the design optimization should be noted. First, the shape and amplitude of the imperfection were assumed to be the critical buckling mode and one shell thickness, respectively. The design method was focused on eliminating the sensitivity of axially loaded cylindrical shells to traditional imperfections, i.e., geometric mid-surface imperfections, which have been commonly studied in the literature on thin shell buckling. Because the actual imperfections of wavy shells were unknown until these shells were fabricated, the imperfection shape was chosen to be the first (critical) buckling mode which is one of the worst imperfections (Jones, 2006; Hilburger et al., 2006). The imperfection amplitude was set equal to the nominal shell thickness. According to Koiter (1963) this amplitude could cause a fivefold decrease in the buckling load and hence provides a significant challenge for when searching for imperfection insensitive designs. Both positive and negative signs for the imperfection amplitude were used, to consider the three types of buckling (stable, unstable, and asymmetric buckling) which may be exhibited by different shell designs.

Second, axial compression was applied as a uniformly distributed axial load. Here it should be noted that axial compression could be applied either as a uniform axial load or as a uniform end-shortening. These two approaches are not equivalent in shells with symmetry-breaking cross-sections, hence they will result in different buckling loads. In general, applying a uniform end-shortening will lead to higher buckling loads than applying a uniform axial load, because a uniform end-shortening results in larger loads over longitudinal sections of the shell that, due to a smaller radius of curvature, have a higher buckling stress. In our previous studies, the loading condition that leads to lower overall buckling loads, i.e., uniform axial load, was used in the optimization. A more detailed study of these two loading conditions is presented in Section 4.

Third, any thickness variations of shell wall and any limits on the material strength were ignored in the optimization in Ning and Pellegrino (2015); however, these two factors are incorporated in the present study.

Table 1
Dimensions of wavy shell designs.

Radius, R	35 mm
Length L	70 mm
Maximum deviation from circle, Δr	1.5 mm

In summary, the optimization problem was formulated as follows:

$$\begin{aligned}&\text{Maximize}: \quad \min\,(P_0, P_+, P_-)\\&\quad \text{among all wavy shells with mirror-symmetric}\\&\quad \text{cross-sections, defined by the control variables:}\\&\quad r_{1,i},\ i=1,\ 2,\ 3,\ \ldots\\&\text{that are subject to}:\\&|r_{1,i}-R| \ \le\ \Delta r,\ i=1,\ 2,\ 3,\ \ldots. \qquad (2)\end{aligned}$$

where:

- P_0, P_+, and P_- are respectively the buckling loads of wavy shells with perfect geometry, imperfect geometry with positive imperfection, and imperfect geometry with negative imperfection;
- the positive imperfection is $+t\Phi$ and the negative imperfection is $-t\Phi$. Φ is the normalized critical buckling mode.

2.2. Composite wavy shell

In order to minimize the cost and complexity of the test program, only small scale test samples were built and tested in the present study. The length of the test section of the shell was chosen to be 70 mm, and a square aspect ratio was chosen, i.e., the diameter was equal to the length (70 mm), which is a common choice for studies of shell buckling, see for example Arbocz and Babcock (1968); Davis (1982), and Hilburger et al. (2006). The shell dimensions are summarized in Table 1.

Thin-ply carbon fiber composites provided by the North Thin Ply Technology Company were used. A symmetric six-ply laminate, $[+60^\circ, -60^\circ, 0^\circ]_s$, was found to be sufficiently flexible before curing that it could be used to successfully make shells with the required corrugated shapes. The particular prepregs that were chosen were 30 µm thick unidirectional laminae of T800 carbon fibers and ThinPreg 120EPHTg-401 epoxy with a fiber volume fraction of 50%. The total thickness of the laminate is 30 µm. The following nominal lamina properties were measured: $E_{1,nom} = 127.9$ GPa, $E_{2,nom} = 6.49$ GPa, $G_{12,nom} = 7.62$ GPa, and $\nu_{12,nom} = 0.354$. It should be noted that these properties were obtained based on the nominal lamina thickness, 30 µm.

The stiffness of a composite laminate can be described by the "ABD" matrix (Daniel and Ishai, 2006):

$$\begin{bmatrix} A_{xx} & A_{xy} & A_{xs} & B_{xx} & B_{xy} & B_{xs}\\ A_{yx} & A_{yy} & A_{ys} & B_{yx} & B_{yy} & B_{ys}\\ A_{sx} & A_{sy} & A_{ss} & B_{sx} & B_{sy} & B_{ss}\\ B_{xx} & B_{xy} & B_{xs} & D_{xx} & D_{xy} & D_{xs}\\ B_{yx} & B_{yy} & B_{ys} & D_{yx} & D_{yy} & D_{ys}\\ B_{sx} & B_{sy} & B_{ss} & D_{sx} & D_{sy} & D_{ss} \end{bmatrix} \begin{bmatrix} \epsilon_x^o\\ \epsilon_y^o\\ \gamma_s^o\\ \kappa_x\\ \kappa_y\\ \kappa_s \end{bmatrix} = \begin{bmatrix} N_x\\ N_y\\ N_s\\ M_x\\ M_y\\ M_s \end{bmatrix}, \qquad (3)$$

or, in brief,

$$\begin{bmatrix} A & B\\ B & D \end{bmatrix} \begin{bmatrix} \epsilon^o\\ \kappa \end{bmatrix} = \begin{bmatrix} N\\ M \end{bmatrix}, \qquad (4)$$

where ϵ^o and κ are the mid-plane strains and curvatures, respectively. N and M denote the mid-plane forces per unit length and the moments per unit length. The A matrix is the extensional stiffness matrix, relating in-plane loads to in-plane strains; the D matrix is the bending stiffness matrix, relating moments to curvatures; and the B matrix is the coupling stiffness matrix. The ABD matrix of the laminate was calculated:

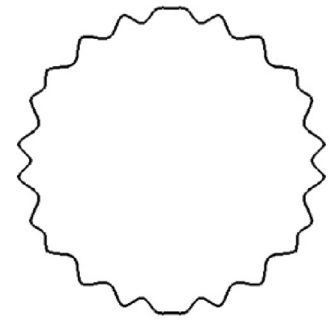

Fig. 3. Cross-section of chosen shell design.

$$ABD = \begin{pmatrix} 9.919\times10^6 & 2.670\times10^6 & 0 & 0 & 0 & 0\\ 2.670\times10^6 & 9.919\times10^6 & 0 & 0 & 0 & 0\\ 0 & 0 & 3.625\times10^6 & 0 & 0 & 0\\ 0 & 0 & 0 & 0.0108 & 0.0099 & 0.0034\\ 0 & 0 & 0 & 0.0099 & 0.0373 & 0.0081\\ 0 & 0 & 0 & 0.0034 & 0.0081 & 0.0125 \end{pmatrix}, \qquad (5)$$

where the units of the A and D matrices are N/m and Nm, respectively.

The method of Section 2.1 was used to design a six-ply composite imperfection insensitive wavy shell for our tests. The design used 16 control points in the first quadrant and two planes of mirror symmetry for the cross-section shape. The cross-section of the shell is shown in Fig. 3, and the radial positions of the 16 control points are presented in Table 2. This design has buckling loads of $P_0 = 14.981$ kN, $P_+ = 14.908$ kN, and $P_- = 14.897$ kN. Therefore, this design has a sensitivity of 0.994 to mid-surface geometric imperfections. It should be noted that these buckling loads were obtained based on the critical-mode imperfection, uniform axial load, and nominal shell thickness.

It should be noted that the present study has focused on experiments on short shells, with a length-to-diameter ratio (L/D) of 1. Preliminary numerical studies on the effects of varying L were carried out by Ning (2015). It was found that in shells with the same cross-section as Fig. 3 but $L/D = 2$ the knockdown factor decreased from 0.994 to 0.708. However, when a new optimization of the cross-section was carried out specifically for the case $L/D = 2$, using the method described in Section 2.1, it was found that the knockdown factor increased to 0.993. The interested reader is referred to Ning (2015) for more details.

2.3. Shell manufacture

Three wavy shells were manufactured by laying the composite laminate on a wavy steel mandrel (shown in Fig. 4), which had been made by a wire electrical discharge machining machine, followed by autoclave curing. To facilitate the separation of the shell from the mandrel, a layer of 12.5-micron thick Kapton film was used between the laminate and the mandrel. This film remained bonded to the shell after curing and, being much thinner and softer than the composite material, had a negligible effect on the buckling load. Calculations showed that the change of buckling loads due to the Kapton film was less than 0.1%, hence the influence of the Kapton film was ignored.

The laminate was held under vacuum through the entire cure process. Before separating the shell from the mandrel after curing, a metal blade and sand paper were used to trim and grind the two

Table 2
Radial positions of 16 control points of chosen shell design.

Point	1	2	3	4	5	6	7	8	9	10	11	12	13	14	15	16
$r_i - R$ [mm]	−1.5	1.5	−1.5	−1.5	1.5	0	1.5	−1.5	−1.5	1.4	−1.5	−1.2	1.5	−1.5	1.1	1.4

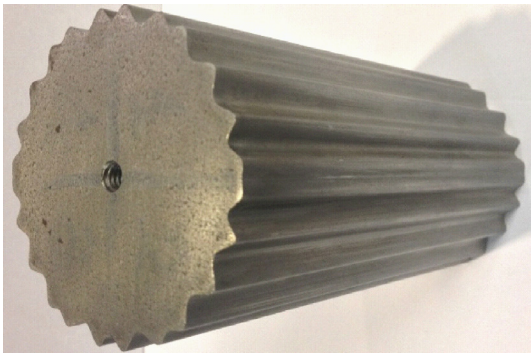

Fig. 4. Steel mandrel.

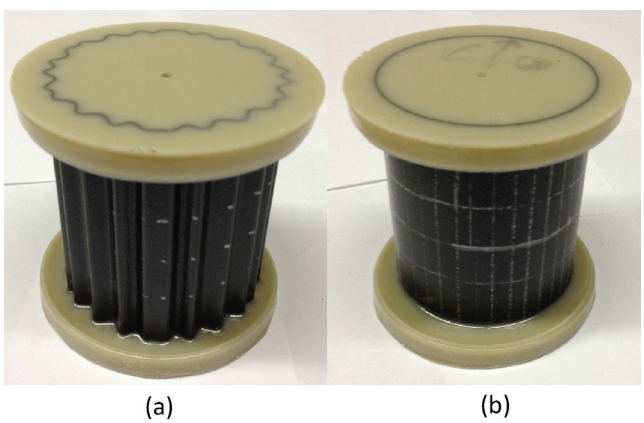

Fig. 5. (a) Wavy shell and (b) circular shell with potted ends.

ends of the shell to match the ends of the mandrel. This ensured that the ends of each shell were flat and parallel to each other.

In addition to the three composite wavy shells, two circular cylindrical shells that had the same length ($L = 70$ mm), radius ($R = 35$ mm), and material as the wavy shells were also made.

Clamped boundary conditions were obtained by potting the ends of the shells into room temperature cure epoxy EpoxA-cast 650, a mineral filled general purpose casting epoxy made by Smooth-On, Inc. It has a low shrinkage and a low mixed viscosity for minimal air entrapment. The epoxy was poured into a plastic cup with open ends held on a piece of flat glass, which guaranteed that the cured epoxy had a flat bottom surface. To avoid large distortions during the potting process, the shells were slid down on the mandrel which was held on a fixture and then slowly lowered into the epoxy, when potting the first end. The potted wavy and circular shells are shown in Fig. 5.

3. Geometric imperfections

This section first presents the thickness distributions of the three wavy shells. A photogrametry technique for measuring the mid-surface imperfections and the results of these measurements are then presented.

3.1. Thickness distributions

The thickness distributions were measured using a micrometer before potting the shells into epoxy. The thickness was measured

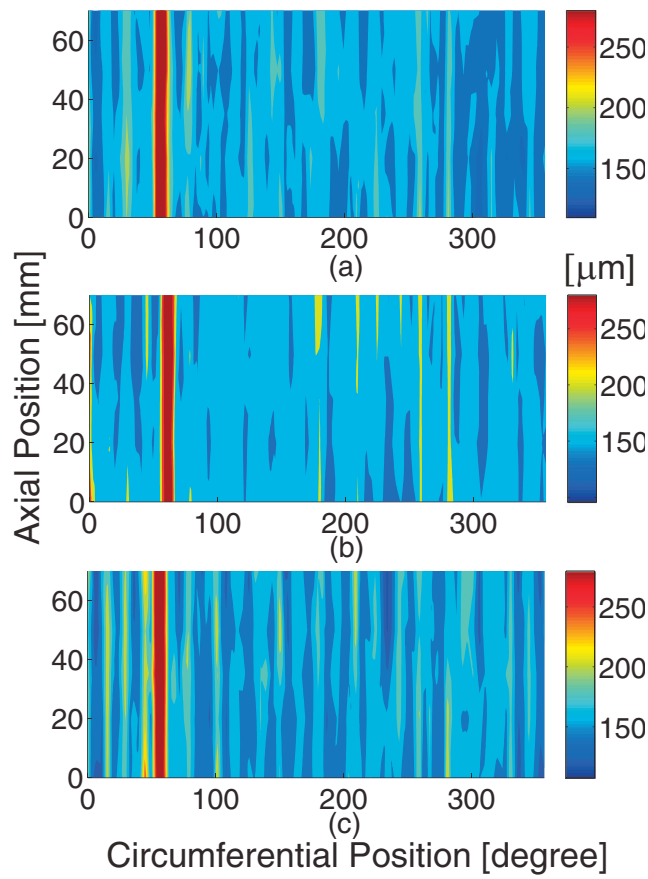

Fig. 6. Thickness distributions of wavy shells (a) 1, (b) 2, and (c) 3.

Table 3
Measured thickness distributions of wavy shells.

Wavy Shell	Thickness [μm]
1	166± 16
2	166± 22
3	165± 19

at the heights of 0 cm, 2 cm, 5 cm and 7 cm on each hill, valley, as well as the middle points between the hill and valley of each corrugation, were measured. The thickness at the height of 3.5 cm on the middle points between the hill and valley of each corrugation was also measured. Fig. 6 shows the thickness distributions of the three wavy shells. The mean and standard deviations for the thickness are listed in Table 3. Note that the average thicknesses of the wavy shells were around 166 μm, 7.8% thinner than the nominal thickness of 180 μm. Each shell contained a narrow, longitudinal band with thickness of around 300 μm, formed by the overlap of the two ends of the composite laminate, as well as regions where of much smaller thickness than the average value. The influence of thickness non-uniformity is discussed in Section 4.4.

3.2. Measurement of mid-surface imperfections

The three-dimensional survey technique, which uses a probe to scan a shell surface, is the main method for measuring shell

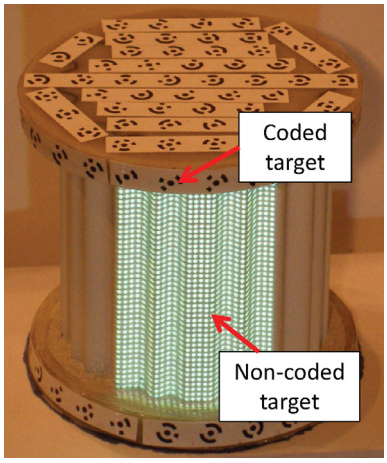

Fig. 7. Coded and non-coded targets.

imperfections (Singer et al., 2002; Arbocz and Williams, 1977; Verduyn and Elishakoff, 1982). However, this is not a feasible method to measure the wavy shells described in Section 2.2 because they are rather thin and even a small pressure applied by the probe would introduce deformations of the thin shell wall, resulting in inaccurate measurements. Therefore, a non-contact photogrammetry technique was chosen to measure the shell geometry.

The commercial photogrammetry software Photomodeler 6 (EOS Systems, 2004) was used with two types of targets. Coded targets are black circular spots surrounded by black segments of rings. Each coded target is unique and hence can be detected by the software. The coded targets were attached to the top and lateral surfaces of the cured epoxy base, see Fig. 7. Non-coded targets are circular dots projected onto the shell surface by means of an LCD projector. A thin layer of white paint was sprayed on the shell surface to increase the contrast and facilitate the detection of the non-coded targets.

There are three steps involved in a measurement. In the first step the coded targets were photographed by a single Olympus SF350 camera (8 megapixels) and correlated by Photomodeler 6 to define a global coordinate system. The shells were rotated between 18 and 23 times such that all coded targets can be photographed by the camera. The photos were processed with Photomodeler 6. All photos included the coded targets on the top surface of the epoxy base, to act as fiducials in the final correlation of all data. Three non-collinear coded targets on the top surface were picked to define the $O - X - Y$ plane, and the distance between two of these points provided a scale for the measurements.

The second step obtained the positions of the non-coded targets, using three cameras pointed in different directions. Photomodeler 6 was used to correlate the coded and non-coded targets in these three photos with all the photos taken in the first step to calculate their coordinates in the global coordinate system. The non-coded targets were projected onto a rectangular area of the shell that include three or four corrugations, as seen in Fig. 7, and the shell was rotated multiple times to obtain the complete geometry.

The third step consists in computing the shell mid-surface imperfections. It should be noted that the non-coded targets lie on the shell outer surface. Therefore, the procedure described above obtained the shell outer-surface imperfections, from which the mid-surface imperfections were obtained by subtracting the thickness variations. In this step, only the non-coded targets were used to compute the mid-surface imperfection. The accuracy of the imperfections measured in this way was better than 20 μm.

The outer-surface imperfections were calculated by comparing the measured positions of the non-coded targets to the outer-surface of an imaginary perfect wavy shell. The position of the perfect wavy shell was determined by finding the best-fit shell to the measured data (Singer et al., 2002). This process is schematically shown in Fig. 8.

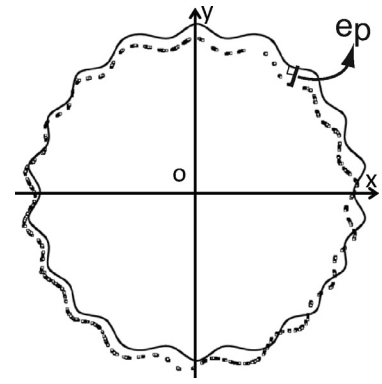

Fig. 8. Schematic of finding the best-fit position of measured shells. e_p is the normal distance between the pth measured point and the corresponding point on the perfect shell.

The method of least squares was adopted to minimize the sum of the squares of the normal distances from the measured points to the reference perfect cylinder by varying the rigid-body translations and rotations of the perfect shell (Arbocz and Babcock, 1968; Cartalas et al., 1990; Hilburger et al., 2006). A three-parameter transformation was defined in terms of translations in the x and y directions and a rotation with respect to the z-axis, and the square of the distance between the measured and the reference shapes was computed. The coordinate transformation was determined by solving the following minimization problem:

$$\begin{aligned} &\text{Minimize}: \sum_{p=1}^{N_p} e_p^2(T_x, T_y, R_z) \\ &\text{Subject to}: \quad (1) \quad |T_x| \le 10 \text{ mm} \\ &\qquad\qquad\quad (2) \quad |T_y| \le 10 \text{ mm} \\ &\qquad\qquad\quad (3) \quad |R_z| \le \frac{\pi}{2} \end{aligned} \tag{6}$$

where e_p, T_x, T_y and R_z are the normal distance, translations in the x and y directions, and rotation with respect to the z-axis, respectively. N_p denotes the total number of measured points. Before running the minimization problem, the perfect wavy shell was manually moved to a position close to the measured cluster of points, in order to achieve faster convergence. Therefore, only small ranges for T_x, T_y and R_z, as shown in the constraints in Eq. (6), were needed. Considering that the explicit mathematical form for $\sum_{p=1}^{N_p} e_p^2(T_x, T_y, R_z)$ was unknown, the minimization problem was solved by the evolutionary algorithm CMA-ES (Hansen et al., 2003; Hansen, 2011; 2012) for convenience.

3.3. Mid-surface imperfection

The mid-surface imperfections are plotted in Fig. 9; the imperfection amplitudes are listed in Table 4.

Mid-surface imperfections can be represented by Fourier series in order to analyze and compare different imperfections. A commonly used form of Fourier series for decomposing initial imperfections is the half-wave cosine Fourier expansion (Arbocz and Babcock, 1968; Singer et al., 2002):

$$\omega(x, \theta) = t_{nom} \sum_{k=0}^{M} \sum_{l=0}^{M} \cos\left(\frac{k\pi x}{L}\right)[A_{kl}\cos(l\theta) + B_{kl}\sin(l\theta)] \tag{7}$$

where L and t_{nom} are the shell length and nominal thickness, respectively. x and θ denote the axial and circumferential

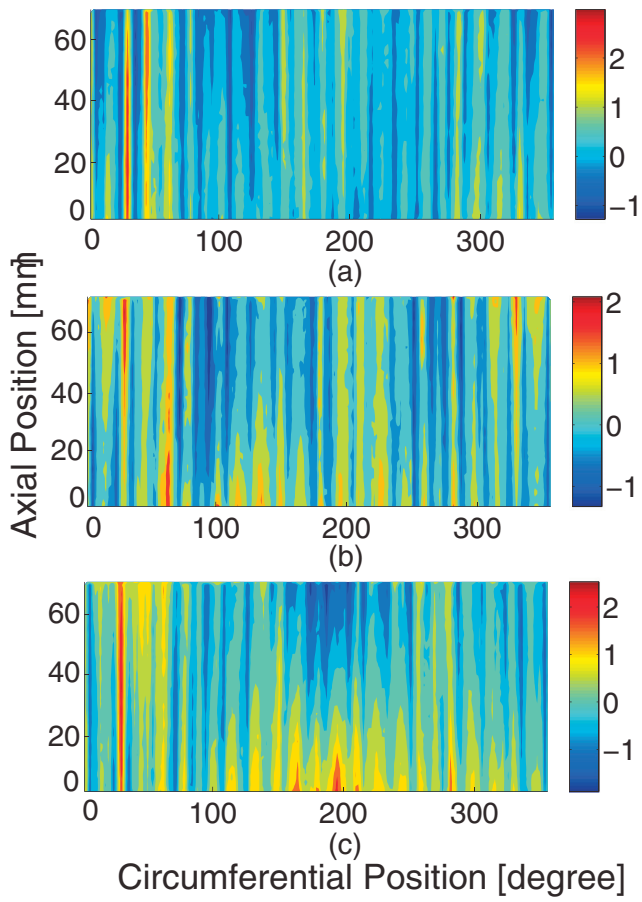

Fig. 9. Mid-surface imperfection ratio (imperfection divided by nominal thickness) distributions of wavy shells (a) 1, (b) 2, and (c) 3.

Table 4
Measured amplitudes of mid-surface imperfections of wavy shells. μ is the ratio between the imperfection amplitude and nominal shell thickness 180 μm.

Wavy Shell	Imperfection Amplitude [μm]	μ
1	536	2.98
2	374	2.08
3	455	2.53

coordinates. k and l are the wave numbers of axial half-cosine waves and circumferential full-waves, respectively. The Fourier coefficients are given by Cartalas et al. (1990):

$$
\begin{aligned}
A_{00} &= \frac{1}{2\pi L t_{nom}} \int_0^L \int_0^{2\pi} \omega(x,\theta)\ dx\ d\theta \\
A_{k0} &= \frac{1}{\pi L t_{nom}} \int_0^L \int_0^{2\pi} \omega(x,\theta)\ \cos\left(\frac{k\pi x}{L}\right)\ dx\ d\theta, \quad k > 0 \\
A_{0l} &= \frac{1}{\pi L t_{nom}} \int_0^L \int_0^{2\pi} \omega(x,\theta)\ \cos(l\theta)\ dx\ d\theta, \quad l > 0 \\
A_{kl} &= \frac{2}{\pi L t_{nom}} \int_0^L \int_0^{2\pi} \omega(x,\theta)\ \cos\left(\frac{k\pi x}{L}\right)\ \cos(l\theta)\ dx\ d\theta, \\
&\quad k > 0,\ l > 0 \\
B_{k0} &= 0, \quad k \geq 0 \\
B_{0l} &= \frac{1}{\pi L t_{nom}} \int_0^L \int_0^{2\pi} \omega(x,\theta)\ \sin(l\theta)\ dx\ d\theta, \quad l > 0 \\
B_{kl} &= \frac{2}{\pi L t_{nom}} \int_0^L \int_0^{2\pi} \omega(x,\theta)\ \cos\left(\frac{k\pi x}{L}\right)\ \sin(l\theta)\ dx\ d\theta, \\
&\quad k > 0,\ l > 0
\end{aligned}
\tag{8}
$$

The amplitude of each imperfection component can be computed from:

$$\xi_{k,l} = \sqrt{A_{kl}^2 + B_{kl}^2} \tag{9}$$

The mid-surface imperfections in Fig. 9 were decomposed according to Eqs. 8 and 9. The imperfection amplitudes for components $k = 0$, $k = 1$, and $l = 0$ to $l = 50$ are plotted in Fig. 10. The amplitudes of $k \geq 2$ components for all l's ranging from 0 to 50 were much smaller than $k \leq 1$, and thus they are not shown in the figure.

For example, the peak, second, and third imperfection components of wavy shell 1 are respectively $A_{0,0}$, $A_{0,24}\cos(24\theta) + B_{0,24}\sin(24\theta)$, and $A_{0,22}\cos(22\theta) + B_{0,22}\sin(22\theta)$, indicating that the major imperfection components of wavy shell 1 are uniform along the axial direction. The $k = 0$, $l = 22$ and $k = 0$, $l = 24$ components are among the largest three imperfection components of wavy shell 2. However, both wavy shell 2 and 3 have large axial half-cosine ($k = 1$) imperfections.

4. Refined predictions for wavy shells

The simulations carried out during the initial experiment design phase, presented in Section 2.1, were refined by accounting for the measured thickness distribution and the mid-surface imperfections of each tested wavy shell.

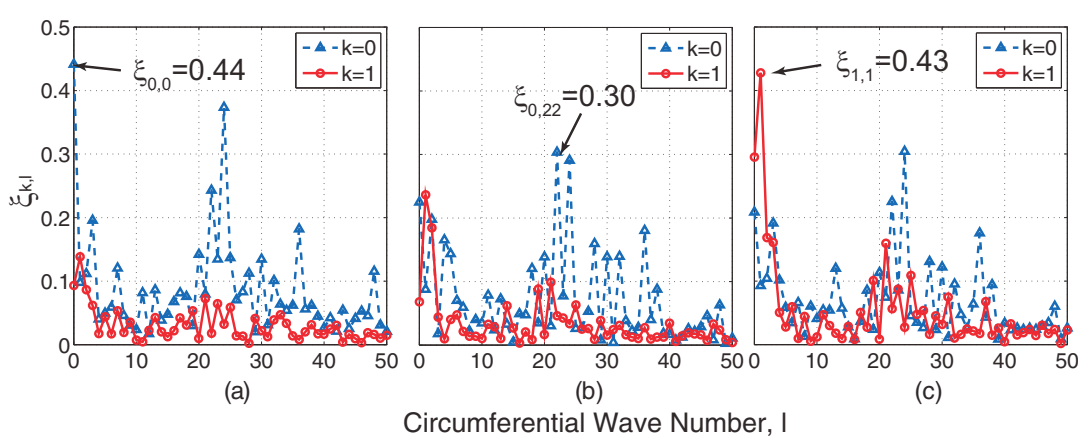

Fig. 10. Fourier components of mid-surface imperfections of wavy shells (a) 1, (b) 2, and (c) 3.

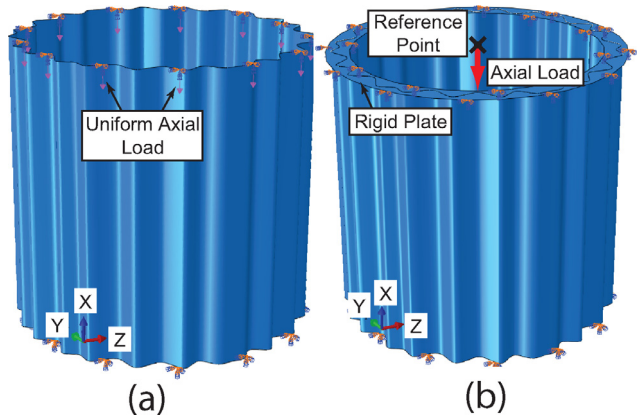

Fig. 11. Abaqus models for (a) uniform axial load and (b) uniform end-shortening.

4.1. Adjusted material properties

The material properties in Eq. (5) were computed based on the nominal shell thickness 180 μm; however, the measured average shell thickness of the three wavy shells was 166 μm. Hence, it is necessary to modify the ABD matrix to account for the reduction in shell thickness. This study followed Hilburger and Starnes (2001) who assumed that any variations in shell thickness result from a variation in only the volume of epoxy rather than the fiber volume, and used the rule of mixtures to adjust the lamina properties for the measured shell thickness. Hence, the modified lamina properties were obtained from:

$$\begin{aligned} V_f &= \frac{V_{f,nom}}{\alpha} \\ E_1 &= \frac{1}{\alpha} E_{1,nom} \\ E_2 &= \frac{\alpha(1-V_{f,nom})}{\alpha - V_{f,nom}} E_{2,nom} \\ G_{12} &= \frac{\alpha(1-V_{f,nom})}{\alpha - V_{f,nom}} G_{12,nom} \\ \nu_{12} &= \nu_{12,nom} \end{aligned} \tag{10}$$

where α is the ratio between the measured and nominal laminate thickness, and α is 0.922 for the wavy shells tested in the present study. Using the classical lamination theory, the modified ABD matrix for $\alpha = 0.922$ was calculated as:

$$ABD(\alpha = 0.922) = \begin{pmatrix} 9.928\times10^6 & 2.668\times10^6 & 0 & 0 & 0 & 0 \\ 2.668\times10^6 & 9.928\times10^6 & 0 & 0 & 0 & 0 \\ 0 & 0 & 3.630\times10^6 & 0 & 0 & 0 \\ 0 & 0 & 0 & 0.0093 & 0.0084 & 0.0029 \\ 0 & 0 & 0 & 0.0084 & 0.0317 & 0.0069 \\ 0 & 0 & 0 & 0.0029 & 0.0069 & 0.0106 \end{pmatrix} \tag{11}$$

where the units of the A and D matrices are N/m and Nm, respectively.

4.2. Finite element models

Recall from Section 2.1 that in the Abaqus model of the shell, the bottom edge is fully clamped and the top edge nodes have only one degree of freedom, i.e., the displacement in the axial direction. Also recall that there are two ways to apply axial compression: uniform axial load and uniform end-shortening, as shown in Fig. 11. Both loading conditions were considered and uniform end-shortening was chosen as it provides a more accurate representation of the experiments.

Table 5
Computed buckling loads for wavy shells of uniform thickness and mid-surface imperfection based on critical buckling mode. μ is the imperfection amplitude divided by the nominal shell thickness, $t_{nom} = 180$ μm.

	P_0 [kN]	μ	$\min(P_+, P_-)$ [kN]
Uniform axial load	10.46	2	10.34
		2.5	10.37
		3	10.39
Uniform end-shortening	10.44	2	13.06
		2.5	12.98
		3	12.91

In order to set up this condition, a rigid plate was defined and a concentrated axial load was applied to the rigid plate through a reference point as illustrated in Fig. 11 (b). The rigid plate can only move axially without any transverse displacements or rotations, i.e., $U_y = U_z = R_x = R_y = R_z = 0$. The top edge of the shell was constrained to the rigid plate by the "tie constraint" in Abaqus CAE/Standard (Simulia Corp, 2011), which can guarantee that the top edge has the same translational displacements and rotations as the rigid plate. Therefore, the top edge of the shell can only move along the axial direction. The bottom edge of the shell was fully clamped, i.e., $U_x = U_y = U_z = R_x = R_y = R_z = 0$.

The buckling loads were computed by carrying out a load-displacement arc-length incremental, geometrically nonlinear analysis, using the Riks solver in Abaqus CAE/Standard. The first limit load in the load-displacement curve was defined as the buckling load. The increments of the axial load in the analysis were limited between 50 N and 100 N. All analysis models consisted of around 30,000 reduced integration quadratic thin-shell elements (S8R), where the element size was determined by a mesh sensitivity study.

4.3. Buckling loads based on uniform thickness and critical-mode imperfections

The buckling loads of the three wavy shells were computed using uniform thickness models with the measured average shell thickness of 166 μm. The imperfection shape was chosen to be the critical buckling mode, obtained from a linear eigenvalue buckling analysis in Abaqus/Standard, and several different imperfection amplitudes were considered. The imperfection was introduced in the model by superposing the critical buckling mode on the mesh of the perfect shell and modifying the positions of its nodes in the model. Imperfections with both positive and negative amplitudes were considered.

Simulations for both cases of uniform axial load (Fig. 11 (a)) and uniform axial end-shortening (Fig. 11 (b)) were carried out using the modified ABD matrix in Eq. (11). The buckling loads of geometrically perfect shells, P_0, and imperfect shells of various imperfection amplitudes, P_1 and P_+, are summarized in Table 5.

The buckling loads of the perfect shells for the cases of uniform axial load and uniform end-shortening were very close. The knockdown factors for the cases of uniform axial load are 0.991 or even higher for larger imperfections. In the case of imperfect wavy shells subject to uniform end shortening the buckling loads are over 20% higher than the perfect shell.

Table 6
Computed buckling loads that account for measured thickness only. The shells were under uniform end-shortening.

Wavy Shells	Buckling Loads
Wavy shell 1	10.36 kN
Wavy shell 2	10.24 kN
Wavy shell 3	9.61 kN

Table 7
Computed buckling loads that account for both measured thickness and mid-surface imperfection distributions. The shells were under uniform end-shortening.

Wavy Shells	Buckling Loads
Wavy shell 1	13.13 kN
Wavy shell 2	12.85 kN
Wavy shell 3	12.58 kN

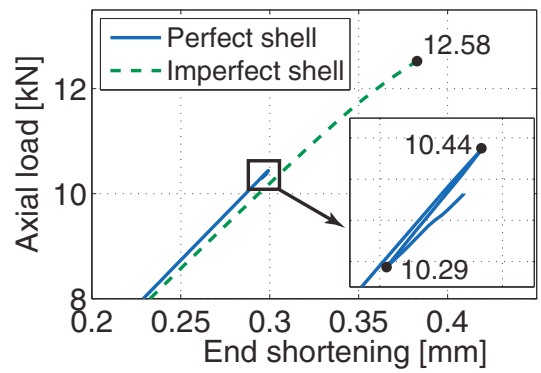

Fig. 12. Computed load versus end shortening curves for perfect shell and imperfect wavy shell 3.

It is challenging to apply a uniform axial loading in an experiment on a wavy shell. Axial compression is usually applied by means of a stiff platen connected to the cross bar of a materials testing machine, which moves in the axial direction; see for example Wu et al. (2013); White et al. (2015), and Hilburger et al. (2012). Therefore, the present study adopted this established experimental setup, and the uniform end-shortening condition shown in Fig. 11 (b) was used for comparison to the experiments. It should be noted that, although ideally the platen should not rotate at all, in real situations it may rotate by a small amount due to misalignments between shell and platen, non-uniform contact surface, etc. (Wu et al., 2013; White et al., 2015; Hilburger and Starnes, 2001) It was found that the influence of the rotation of the upper platen was rather small for the designed wavy shells, and more details are provided in Section 4.5.

4.4. Buckling loads based on actually measured thickness and imperfections

The measured thickness and imperfection distributions shown in Figs. 6 and 9 were incorporated in the finite element models to further improve their accuracy. The non-uniform thickness was defined by assigning a modified local ABD matrix to the shell sections. The shell model was partitioned into around 600 patches, and the thickness in each patch was assumed uniform and equal to measured local average thickness within the patch. The ratio between the local average thickness and the nominal thickness, α, was first computed, and the lamina properties were adjusted using Eq. (10). The local ABD matrix was calculated by using the classical lamination theory and then assigned to the corresponding patch in the model.

To study the influence of non-uniform thickness, the measured thickness distributions (Fig. 6) were incorporated in the finite element models using the method described above. The mid-plane imperfections were not considered. The results are presented in Table 6; recall that the buckling load of the perfect wavy shell, which has a uniform thickness of 166 µm, is 10.44 kN. Therefore, even though each shell contains a thicker longitudinal band, the buckling loads in Table 6 are all lower than the uniform thickness value. The largest decrease was 8% for wavy shell 3, indicating that the influence of non-uniform thickness is rather small.

The buckling loads of the imperfect shells with both non-uniform thickness and mid-surface imperfections were computed, and the results are presented in Table 7. For reference, recall that the buckling load of the perfect wavy shell is 10.44 kN. Note that the buckling loads after introducing the imperfections are significantly larger, showing that the wavy shells were not sensitive to mid-plane imperfections.

Typical load versus end shortening curves are plotted in Fig. 12. Note that the perfect shell in the plot is the shell with uniform thickness of 166 µm and no mid-surface imperfection. The load vs. end shortening curve for the imperfect shell was computed based on the measured non-uniform thickness and mid-surface imperfection of wavy shell 3. The perfect shell buckles at 10.44 kN as the axial load drops to 10.29 kN when it reaches the first limit load, as shown in the detail image. This is a nearly stable postbuckling behavior. The non-linearity due to imperfections leads to a smooth load-end shortening curve and prevents the decrease in axial load at around 10.44 kN, resulting in a higher buckling load than the perfect wavy shell.

It should be noted that the Riks solver stopped shortly after finding the first limit load. This was not a problem for the analysis, since only the buckling loads, defined as the first limits loads on the equilibrium paths, were of interest for the present study. For the perfect wavy shell, the Riks solver was able to go beyond the first instability, into the postbuckling regime, as shown in Fig. 12. For the imperfect structures, the actually measured failure loads were lower than the computed buckling loads, due to failure of the material, as discussed in Section 4.6.2.

4.5. Buckling loads of wavy shells with upper plate free to rotate

The experiments carried out in this study used uniform end-shortening boundary conditions in which the upper plate was not allowed to rotate, as shown in Fig. 11(b). Simulations with the upper plate free to rotate were also conducted in order to study the influence of the rotation of the upper plate. To achieve this boundary condition, the reference point located at the center of the upper plate was fixed only in the Y and Z directions, i.e. $U_y = U_z = 0$. Therefore, the upper plate can move axially and rotate in all directions. The other parameters and setup in these simulations were the same as for the model shown in Fig. 11(b).

Three sets of simulations were performed for this boundary condition, and the results are summarized in Table. 8. First, the perfect wavy shell with uniform thickness (166 µm) and without mid-plane imperfections was simulated. It was found that the

Table 8
Computed buckling loads for wavy shells with the upper plate free to rotate. The unit is kN.

Perfect Wavy Shell		Non-Uniform Thickness Only	Non-Uniform Thickness and Mid-Plane Imperfection
10.44	Wavy Shell 1	9.98	12.59
	Wavy Shell 1	10.16	12.86
	Wavy Shell 3	9.68	11.95

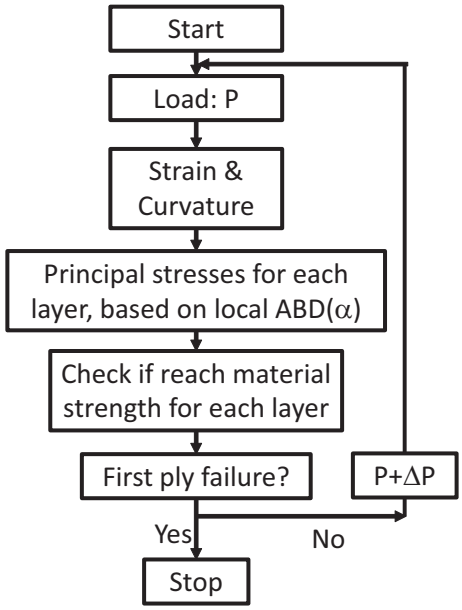

Fig. 13. Flow chart of failure analysis for critical region.

buckling load was 10.44 kN, the same as the value obtained for non-rotating upper plate.

Second, the measured non-uniform thickness distributions were considered, but without including the mid-plane imperfections. The differences between the buckling loads of rotating and non-rotating upper plates (Table. 6) were small, and the maximum difference was only 3.67%. Compared to the perfect wavy shell, the buckling loads slightly decreased due to the non-uniform thickness. The largest decrease was only 8% for wavy shell 3, indicating that the influence of non-uniform thickness is also rather small for this boundary condition.

Third, both the measured thickness distributions and mid-plane imperfections were included in the models. Compared to the non-rotating upper plate in Table. 7, the rotating upper plate slightly reduced the buckling loads. However, its influence was also rather small, and the maximum decrease was only 5%. Recall that the buckling loads of perfect wavy shell is 10.44 kN. Therefore, the shells are not sensitive to mid-plane imperfections for the rotating upper plate boundary condition.

4.6. Failure analysis

4.6.1. Method

The maximum stress theory and the first ply failure theory were used to estimate the failure load of the three wavy shells. To reduce computational time, it was assumed that in each test shell the critical region is the particular element in the finite element mesh where the maximum longitudinal compressive strain occurs. For this specific element a failure analysis was carried out by comparing the longitudinal stress $|\sigma_1|$, transverse stress $|\sigma_2|$, and shear stress $|\tau|$ in each layer to the longitudinal compressive strength F_{1c}, transverse compressive strength F_{2c}, and shear strength F_6. The failure analysis procedure is illustrated in Fig. 13. The analysis was repeated until any one of the stress components reached the corresponding strength.

The lamina stresses can be computed from (Daniel and Ishai, 2006):

$$[\sigma]^k_{1,2} = [T]^k([Q]^k_{x,y}[\varepsilon^o]_{x,y} + z[Q]^k_{x,y}[\kappa]_{x,y}) \tag{12}$$

where $[T]^k$ and $[Q]^k_{x,y}$ are the transformation matrix and transformed stiffness matrix of the kth layer:

$$[T]^k = \begin{pmatrix} \cos^2\theta_k & \sin^2\theta_k & 2\cos\theta_k\sin\theta_k \\ \sin^2\theta_k & \cos^2\theta_k & -2\cos\theta_k\sin\theta_k \\ -\cos\theta_k\sin\theta_k & \cos\theta_k\sin\theta_k & \cos^2\theta_k - \sin^2\theta_k \end{pmatrix} \tag{13}$$

$$[Q]^k_{x,y} = [T^{-1}]^k \begin{pmatrix} \frac{E_1}{1-\nu_{12}\nu_{21}} & \frac{\nu_{12}E_1}{1-\nu_{12}\nu_{21}} & 0 \\ \frac{\nu_{12}E_1}{1-\nu_{12}\nu_{21}} & \frac{E_2}{1-\nu_{12}\nu_{21}} & 0 \\ 0 & 0 & G_{12} \end{pmatrix} [T]^k \tag{14}$$

Here θ_k denotes the fiber angle of layer k. $[\varepsilon^o]_{x,y}$ and $[\kappa]_{x,y}$ are the transformed mid-surface strain and curvature. z is the distance between the mid-surface of the kth layer and the laminate mid-surface. The strains and curvatures in the critical region for any given load P were obtained from the analysis of Section 4.4, i.e., the shell model that accounts for the measured thickness and mid-surface imperfections. The stresses in each layer were calculated from Eq. (12), using the local $ABD(\alpha)$.

The composite material used in this study consists of nominally 30 μm thick unidirectional laminae of T800 carbon fibers and ThinPreg 120EPHTg-401 epoxy with a nominal fiber volume fraction of 50%. The strength of the lamina was estimated based on the shear strength, $F_{ms} = 94.9$ MPa, of the ThinPreg 120EPHTg-401 epoxy provided by the North Thin Ply Company (The North Thin Ply Company, 2013).

The in-plane shear strength of a unidirectional composite is determined by the matrix shear failure and can be predicted from (Daniel and Ishai, 2006):

$$F_6 = \frac{F_{ms}}{k_\tau} \tag{15}$$

where F_{ms} is the matrix shear strength and k_τ is the shear stress concentration factor. Assuming the shear modulus of the matrix to be much smaller than the shear modulus of fiber, k_τ is given by (Daniel and Ishai, 2006):

$$k_\tau = \frac{1 - V_f}{1 - (4V_f/\pi)^{1/2}} \tag{16}$$

Here the volume fraction V_f accounts for the difference between the measured and nominal thickness, and it can be calculated by Eq. 10.

The longitudinal compressive strength is related to the initial fiber misalignment (Daniel and Ishai, 2006):

$$F_{1c} = \frac{F_6}{\phi} \tag{17}$$

where ϕ is the initial fiber misalignment that was measured as 1.9° for the composite used in the present study.

The transverse compressive strength F_{2c} cannot be estimated. Since F_{2c} is usually in the range of 200 to 228 MPa for carbon/epoxy unidirectional composite (Daniel and Ishai, 2006), the value $F_{2c} = 200$ MPa was assumed.

4.6.2. Results

The ratios between the stress components and the corresponding strengths in the critical region of wavy shell 1 are plotted in Fig. 14. All laminae are subject to compression in both longitudinal and transverse directions. According to Fig. 14, layer 5 (−60°) is predicted to be the first to fail by shearing at about 11.90 kN.

The same analyses were carried out also for wavy shells 2 and 3. It was found that shell 2 would fail by shearing in layer 5 (−60°) at 11.65 kN and shell 3 would fail by shearing in layer 6 (60°) at 11.78 kN.

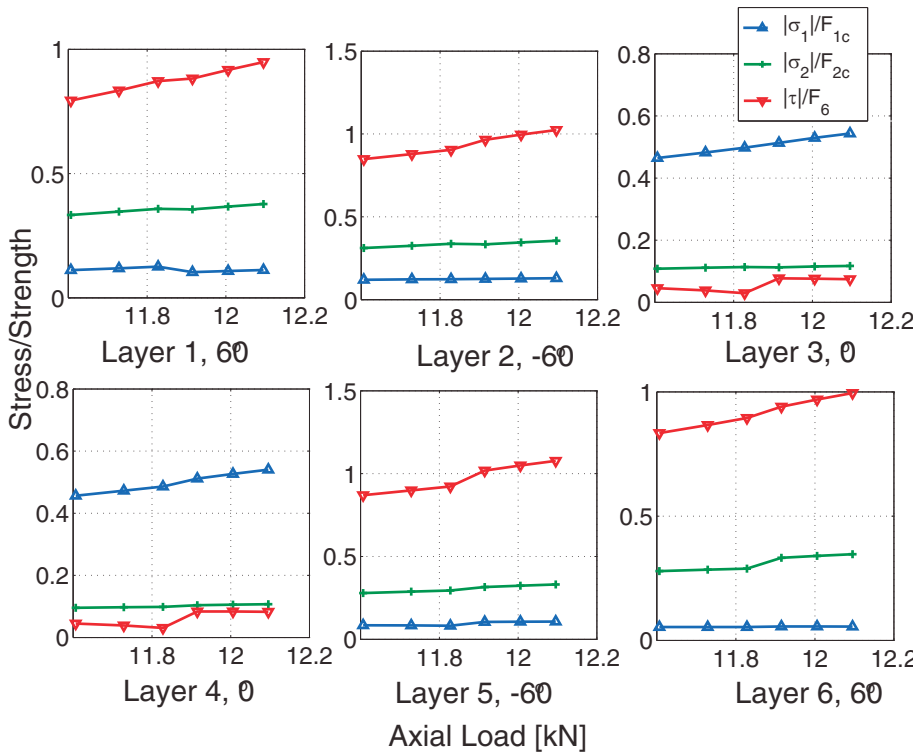

Fig. 14. Ratio between stress and corresponding strength for each layer of laminate of wavy shell 1. Layer 1 is on the outer surface of the shell.

Table 9
Computed critical loads for elastic buckling and material failure.

Wavy Shell	Elastic Buckling [kN]	Material Failure [kN]
1	13.13	11.90
2	12.85	11.65
3	12.58	11.78

The difference between the buckling load and the failure load of a shell should be clarified. The material strength, as well as any kind of nonlinear material behavior, were not considered in any of the buckling analyses, e.g. when computing the load-displacement curves shown in Fig. 12. Table 9 presents the predicted failure loads for the three test wavy shells. The lower of the two values, i.e., the material failure load, will be the actual failure load for each shell. It should be noted that the material failure loads are larger than the buckling load of the perfect wavy shell. Therefore, it is expected that the actual wavy shells will carry at least 100% of the buckling load of the perfect wavy shells, despite the existence of geometric imperfections.

5. Experiments

The three wavy shells, as well as two circular shells were tested. The experimental setup is described and the test results are presented in the following sections.

5.1. Test setup

Fig. 15 shows the setup for the compression tests that were carried out. An Instron 5500 Series materials testing machine with a 50 kN load cell was used to conduct the compression tests. The displacement rate was 1 mm per minute and each test took about 30 seconds. The Vic3D digital image correlation (DIC) system (Correlated Solutions, 2010) was used to record shell deformations before structural collapse. A Phantom v310 high speed camera was used to capture the failure process. The high speed camera was pointed toward the critical region predicted by the analysis of each shell, as discussed in Section 4. The camera speed was 3000 frames per second; the total recording time was about 10 seconds and the recording was manually triggered when the compressive loads reached 9.5 kN.

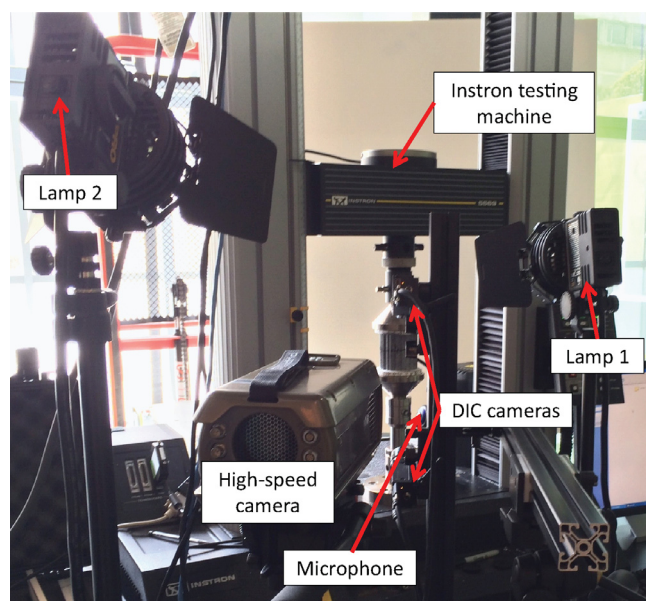

Fig. 15. Experimental setup for compression tests.

5.2. Wavy shells

The buckling loads of the perfect wavy shell and the predicted and measured failure loads of the wavy shells are presented in

Table 10
Predicted and measured failure loads for wavy shells. The buckling load of the perfect wavy shell was computed based on the uniform thickness of 166 μm, which is the measured average thickness.

	Buckling Load [kN]	Failure Load [KN]	
	(Perfect Shell)	Prediction	Test
Wavy Shell 1	10.44	11.90	11.48 ± 0.03
Wavy Shell 2		11.65	11.68 ± 0.03
Wavy Shell 3		11.78	11.30 ± 0.03

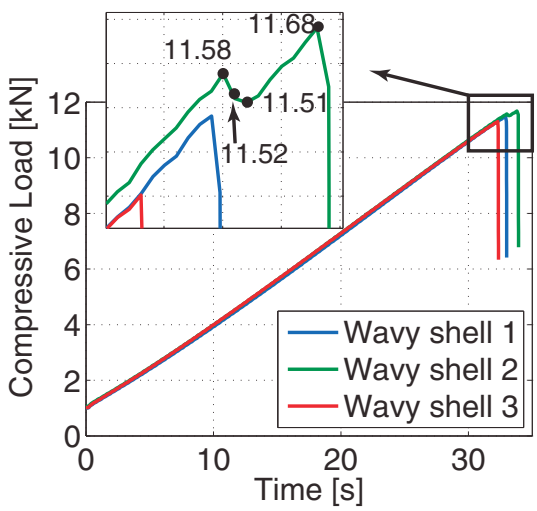

Fig. 16. Load-time curve for wavy shells.

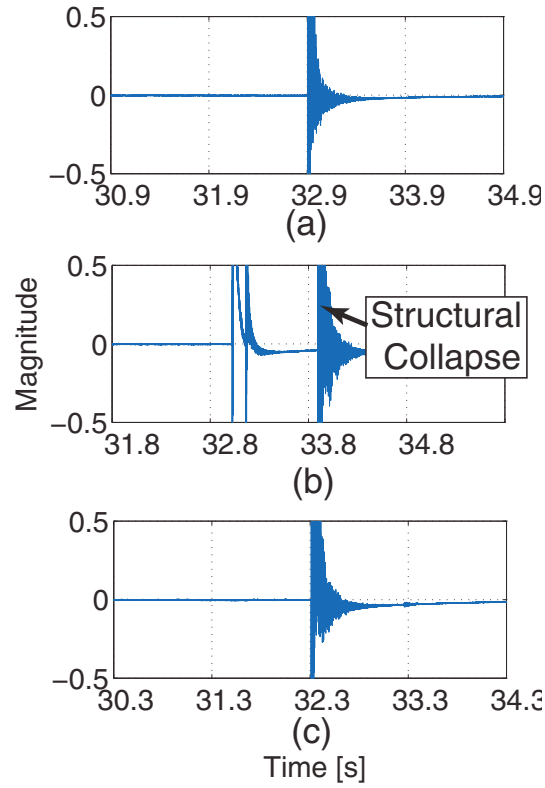

Fig. 17. Acoustic emissions of wavy shells (a) 1, (b) 2, (c) 3.

Table 10. All wavy shells collapsed at loads higher than the buckling load of the perfect wavy shell, confirming that the design is imperfection insensitive. Failure of all three shells was triggered by local material failure, as expected from Section 4.6.2, and it occurred at a load above the predicted buckling load of the geometrically perfect wavy shell. The failure loads of the three shells were very consistent as the maximum load was only 3.4% higher than the minimum one.

The load-time curves of the three wavy shells are plotted in Fig. 16. The compressive load on wavy shells 1 and 3 increased monotonically until they collapsed. The load on wavy shell 2 monotonically increased up to 11.58 kN, and dropped to 11.51 kN before starting to increase again, up to the failure load of 11.68 kN. The accuracy of the measured failure loads in Table 10 was estimated from the accuracy of the load cell, which is ± 0.25% (Instron, 2005).

The acoustic emissions of the three wavy shells during loading were recorded and plotted in Fig. 17. The acoustic emission technique is a convenient tool to study damage initiation and progression (Agarwal et al., 2006). The acoustic emission of wavy shells 1 and 3 shows only one high-amplitude event, corresponding to the structural collapse. The acoustic emission of wavy shell 2 shows three high-amplitude events. The third event corresponds to the structural collapse. The first and second events correspond to the two decreases in load in the load-time curve of this shell, as shown in Fig. 16. It is generally accepted that the fracture of fibers can result in high-amplitude events (Agarwal et al., 2006). Therefore, up to two local fiber-failure events occurred before the final collapse of wavy shell 2. These two local failures did not propagate immediately, and the shell was able to carry higher compressive load until the structural collapse occurred. For wavy shell 2, the load corresponding to the third high-amplitude event (structural collapse) was defined as the failure load.

The deformation of each shell was recorded by the 3D DIC system and a typical out-plane deformation field is plotted in Fig. 18. At small loads the shell expanded outwards (Fig. 18 (a)); at larger loads short wavelength waves in the axial direction appeared in one corrugation (Fig. 18 (b)). Note that these small buckles are clearly visible even when the axial loads were smaller than the buckling load of the perfect wavy shell. And also note that these buckles did not significantly change when the loads were increased beyond the perfect buckling load (Fig. 18 (c)) until the shell failed. These observations suggest that for this imperfection insensitive wavy shell imperfections lead to a stable post-buckling behavior. Similar observations were made on the other two shells, confirming this general trend.

A typical failure process recorded by the high-speed camera on wavy shell 2 is shown in Fig. 19. Fig. 19 (b) shows that the shell failed locally, and this local failure triggered the collapse of the whole structures (Fig. 19 (c)). Significant delamination was observed when the shell was unloaded. These observations conform with the failure predictions in Section 4.

The predicted critical regions, where the axial compressive strain is maximum, along with the observed kind band, are shown by circles in Fig. 20. The initial failure region of wavy shell 1 was not captured by the high-speed camera, but its kink band went through the critical regions predicted by the failure analysis. The initial failure region of wavy shell 2 was located on the same corrugation and at about the same height as predicted by the failure analysis. Three local initial failure regions were observed on wavy shell 3, and two of these regions were on the predicted corrugation. The predicted critical region is about 1 cm higher than the observed initial failure regions.

5.3. Circular cylindrical shells

Two composite circular cylindrical shells of the same radius and length as the wavy shells were made and tested. The thickness

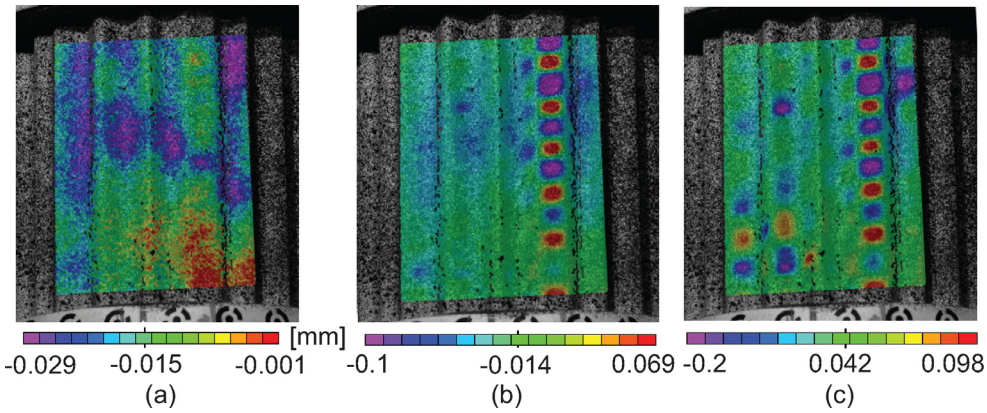

Fig. 18. Out-plane deformation of wavy shell 2 under the axial load of (a) 3.985 kN, (b) 9.536 kN, and (c) 11.626 kN.

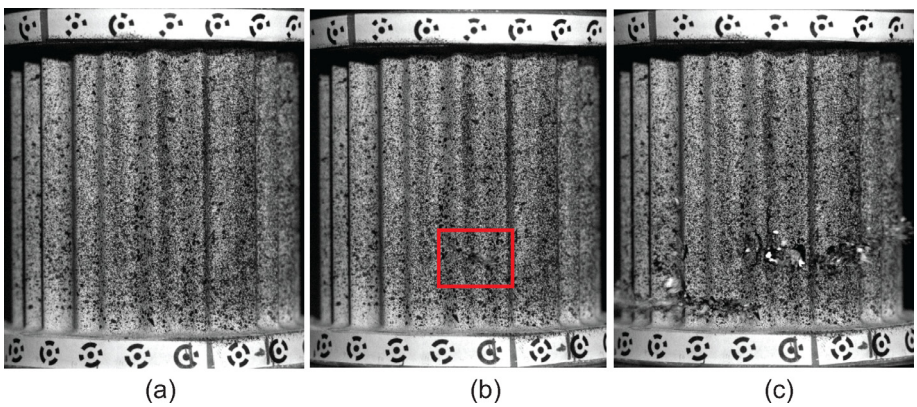

Fig. 19. Three consecutive images of wavy shell 2 recorded by the high speed camera (a) before collapse, (b) during collapse, and (c) after collapse. The initial failure region is marked by a rectangle in (b).

and imperfection distributions had been measured before the compression tests. The results are summarized in Tables 11 and 12. Although the thickness of the circular shells was more uniform and the imperfection amplitudes were smaller than the wavy shells, the measured buckling loads were much lower than the buckling load of the perfect circular cylindrical shell. The average buckling load was 2.21 kN, i.e. only 19.3% of the average failure load of the wavy shells. The highest knockdown factor is only 0.589, indicating a large imperfection sensitivity.

Fig. 21 shows the typical buckling shape of the circular shells. It can be seen that the circular shells buckled into the classical diamond shape. No material failure was observed after unloading, indicating that the circular shells do not fully utilize the strength capacity of the composite material.

6. Conclusion

A precise fabrication technique for cylindrical shells with wavy cross-sections has been developed, and clamped boundary conditions was achieved without introducing large imperfections. Instead of using traditional three-dimensional survey systems, a photogrammetry technique was developed to measure the geometric imperfections of our shells. Three wavy cylindrical shells and two circular cylindrical shells were fabricated and tested.

The behavior of the wavy shells under axial compression was predicted, based on the measured thickness and mid-surface imperfection distributions. The buckling load of the perfect wavy shell, i.e., a wavy shell with uniform thickness of 166 μm and without mid-surface imperfections, was calculated as 10.44 kN. The mid-surface imperfections and non-uniformity of thickness were then incorporated in the finite element models to compute the buckling loads of the three wavy shells that had been built. The predicted buckling loads of the three actual shells, i.e., introducing the measured imperfections in the analysis, were between 12.58 and 13.13 kN. It should be noted that these loads are actually larger than the buckling load of the perfect wavy shell; this result confirmed that the wavy shells are not sensitive to imperfections. The material strength of the manufactured shell was estimated and failure analyses based on the maximum stress failure criterion were carried out. It was predicted that the three wavy shells can reach the material strength and collapse at 11.90, 11.65, and 11.78 kN, respectively, due to shearing in the $\pm 60^o$ layers. The initial failure regions were also predicted.

Compression tests on three wavy shells and two circular cylindrical shells were carried out. A DIC system, high-speed camera, and microphone were employed to record the shell responses during the tests. The three wavy shells collapsed at compressive loads of 11.48 kN, 11.68 kN, and 11.30 kN, respectively. The difference among the three failure loads was only 3.4%, and the overall discrepancy between the measured and predicted failure loads was less than 4.1%. The shell deformations obtained by the DIC system showed that axial waves appeared at a low load and did not change wavelength until the shells collapsed. The high-speed camera was able to capture the initial failure regions of wavy shells 2 and 3. Wavy shell 1 failed by a kink-band going through the predicted critical region. The positions of the initial failure regions matched well with the predicted critical regions. Significant delamination was observed after unloading all the wavy shells.

The measured average buckling load of the circular cylindrical shells was only 19.3% of the average failure load of the wavy

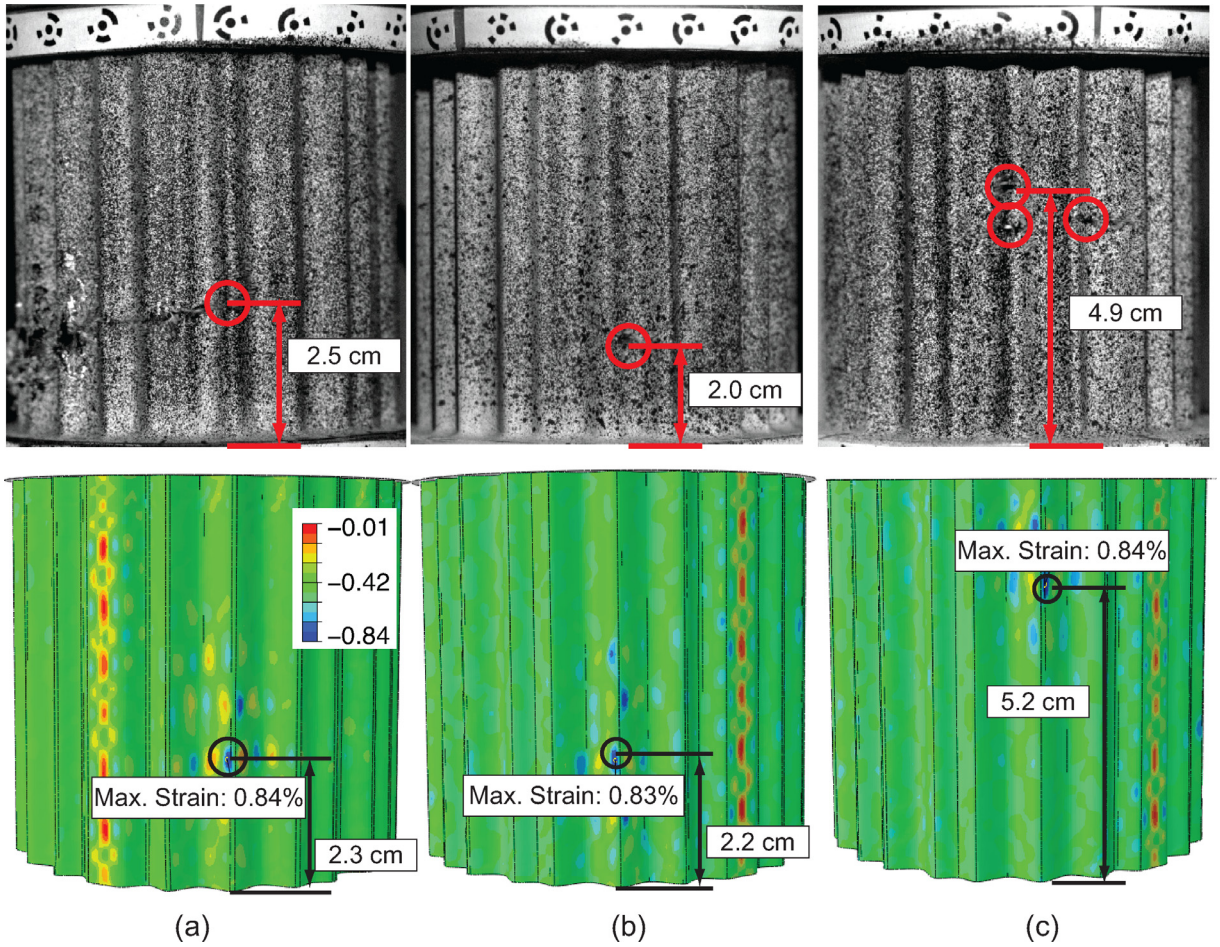

Fig. 20. Comparison of critical regions between experiments (top) and simulations (bottom) for wavy shells (a) 1, (b) 2, and (c) 3. The simulations show the axial strain fields.

Table 11
Measured thickness and imperfections of circular shells.

Shells	Thickness [μm]	Imperfection Amplitude [μm]	μ
Circular shell 1	176± 9	257	1.43
Circular shell 2	176± 13	394	2.19

Table 12
Measured buckling loads and knockdown factors of circular shells.

Shells	Buckling Load (perfect) [kN]	Measured Buckling Load [kN]	Knockdown factor
Circular shell 1	4.06	2.39	0.589
Circular shell 2		2.03	0.499

shells. The highest knockdown factor for the circular shells was only 0.589.

The experiments have shown that the actual wavy shells were able to carry a load larger than the buckling load of the ideal, perfect wavy shell. Therefore, it is concluded that introducing optimal symmetry-breaking wavy cross-section, as proposed in our original study (Ning and Pellegrino, 2015), can eliminate the sensitivity of buckling loads to geometric imperfections. The wavy shells failed at an average load of 11.49 kN, 420% higher than the measured average buckling load of the circular shells, showing that the optimal symmetry-breaking wavy cross-section has significantly improved the load-bearing capability of cylindrical shells.

Fig. 21. Typical buckling shape for circular shells.

It should be noted that in the experiments the upper plates of the shells were not free to rotate and their axial displacements were uniform. The loading method with upper plate free to rotate was not investigated experimentally. However, simulations were carried out to account for the boundary condition of rotating upper plate. It was found that the differences between the buckling loads of rotating plate and non-rotating plate were rather small.

Therefore, it can be confirmed that the improvement in the buckling loads of wavy shells was not due to the method of applying axial compression.

It should also be noted that the experimental studies were limited to short cylindrical shells with length-to-diameter ratio (L/D) of 1 and that numerical studies were performed on shells with L/D up to 2. It would be interesting to carry out experiments on shells with larger L/D in the future. It would also be an interesting future direction to study the performance of wavy shells under other loading conditions, such as external pressure, shearing, and combined loading.

Acknowledgements

We thank Professors P. Ermanni and M.M. Mikulas for help and advice during the course of this study. J. Steeves provided the lamina properties in Section 2.2 and the fiber misalignment data in Section 4.6.1. We thank R. Hurley and Professor J. Andrade for providing access to the high-speed camera. We also thank P. Arakelian, I. Maqueda, and K. Patterson for help and advice regarding shell manufacturing and testing. Financial support from the Resnick Institute at the California Institute of Technology is gratefully acknowledged.

References

Agarwal, B.D., Broutman, L.J., Chandrashekhara, K., 2006. Analysis and Performance of Fiber Composites. John Wiley and Sons, Hoboken, NJ.
Arbocz, J., Babcock Jr, C.D., 1968. Experimental investigation of the effect of general imperfections on the buckling of cylindrical shells. NASA CR-1163.
Arbocz, J., Williams, J.G., 1977. Imperfection surveys on a 10-ft diameter shell structure. AIAA J. 15 (7), 949–956.
Brush, D.O., Almroth, B.O., 1975. Buckling of Bars, Plates, and Shells. McGraw-Hill, New York.
Cartalas, C., van der Hoeven, H.J.C., Klompé, A.W.H., 1990. Guide to the Data Reduction of Imperfection Surveys on Circular Shells. Memorandum M-622, Delft University of Technology, Delft, Netherlands.
Combescure, A., Jullien, J.F., 2015. ASTER shell: a simple concept to significantly increase the plastic buckling strength of short cylinders subjected to combined external pressure and axial compression. Adv. Model. Simul. Eng. Sci. 2 (26), 1–27.
The North Thin Ply Company, 2013. ThinPreg 120 EPHTg/CF Product Datasheet.
Dassault Systèmes Simulia Corp, 2011. Abaqus 6.11 Documentation. Providence, RI.
Daniel, I.M., Ishai, O., 2006. Engineering Mechanics of Composite Materials. Oxford University Press, Oxford.
Davis, R., 1982. Buckling Test of a 3-Meter-Diameter Corrugated Graphite-Epoxy Ring-Stiffened Cylinder. NASA TP-2032.
Hansen, N., 2011. The CMA Evolution Strategy: A Tutorial. Downloaded from https://www.lri.fr/hansen/cmaesintro.html on December 12, 2012.
Hansen, N., 2012. The CMA evolutionary strategy. Downloaded from https://www.lri.fr/hansen/cmaesintro.html on December 12, 2012.
Hansen, N., Müller, S.D., Koumoutsakos, P., 2003. Reducing the time complexity of the derandomized evolution strategy with covariance matrix adaptation (CMA-ES). Evol. Comput. 11, 1–18.
Hilburger, M.W., Haynie, W.T., Lovejoy, A.E., Roberts, M.G., Norris, J.P., Waters, W.A., Herring, H.M., 2012. Subscale and full-scale testing of buckling-critical launch vehicle shell structures. In: Proceedings of the 53rd AIAA/ASME/ASCE/AHS/ASC Structures, Structural Dynamics and Materials Conference. Honolulu, HI, AIAA-2012-1688.
Hilburger, M.W., Nemeth, M.P., Starnes, J.H., 2006. Shell buckling design criteria based on manufacturing imperfection signatures. AIAA J. 44, 654–663.
Hilburger, M.W., Starnes Jr, J.H., 2001. High-fidelity nonlinear analysis of compression-loaded composite shells. In: Proceedings of the 42nd AIAA/ASME/ASCE/AHS/ASC Structures, Structural Dynamics, and Materials Conference. Seattle, WA, AIAA-2001-1394.
Jones, R.M., 2006. Buckling of Bars, Plates, and Shells. Bull Ridge, Blacksburg.
Jullien, J.F., Araar, M., 1991. Towards an optimal cylindrical shell structures under external pressure. In: Jullien, J. (Ed.), Buckling of Shell Structures, on Land, in the Sea, and in the Air. Elsevier, London, pp. 21–32.
Koiter, W.T., 1963. The effect of axisymmetric imperfections on the buckling of cylindrical shells under axial compression. In: Proc. K. Ned. Akad. Wet., Amsterdam, ser. B, vol. 6; also, Lockheed Missiles and Space Co. Rep. 6-90-63-86. Palo Alto, California.
Nemeth, M.P., Starnes, J.H., 1998. The NASA Monographs on Shell Stability Design Recommendations: a Review and Suggested Improvements. NASA TP-1998-206290.
Ning, X., 2015. Imperfection Insensitive Thin Shells. California Institute of Technology. Doctoral dissertation.
Ning, X., Pellegrino, S., 2013. Imperfection-insensitive axially loaded cylindrical shells. In: 54th AIAA/ASME/ASCE/AHS/ASC Structures, Structural Dynamics and Materials Conference. Boston, MA, AIAA-2013-1768.
Ning, X., Pellegrino, S., 2015. Imperfection insensitive axially loaded thin cylindrical shells. Int. J. Solids Struct. 62 (1), 39–51.
Instron Industrial Products, 2005. 2525-800 Series Load Cells.
Scott, N.D., Harding, J.E., Dowling, P.J., 1987. Fabrication of small scale stiffened cylindrical shells. J. Strain Anal. 22, 97–106.
Singer, J., Arbocz, J., Weller, T., 2002. Buckling Experiments: Experimental Methods in Buckling of Thin-Walled Structures: Vol. 2. Wiley, New York.
Correlated Solutions, 2010. Vic-3D reference manual.
EOS Systems, 2004. Photomodeler pro 6, user manual.
Verduyn, W.D., Elishakoff, I., 1982. A Testing Machine for Statistical Analysis of Small Imperfect Shells: Part I. Report LR-357. Delft University of Technology, Delft, Netherlands.
White, S.C., Weaver, P.M., Wu, K.C., 2015. Post-buckling analyses of variable-stiffness composite cylinders in axial compression. Compos. Struct. 123, 190–203.
Wu, K.C., Stanford, B.K., Hrinda, G.A., Wang, Z., Martin, R.A., Kim, H.A., 2013. Structural assessment of advanced composite tow-steered shells. In: Proceedings of the 54th AIAA/ASME/ASCE/AHS/ASC Structures, Structural Dynamics and Materials Conference. Boston, Massachusetts. AIAA-2013-1769.